Aligning Multi-Sequence CMR Towards Fully Automated Myocardial Pathology Segmentation

Wangbin Ding, Lei Li, Junyi Qiu, Sihan Wang, Liqin Huang, Yinyin Chen, Shan Yang, Xiahai Zhuang

Abstract— **Myocardial pathology segmentation (MyoPS) is critical for the risk stratification and treatment planning of myocardial infarction (MI). Multi-sequence cardiac magnetic resonance (MS-CMR) images can provide valuable information. For instance, balanced steady-state free precession cine sequences present clear anatomical boundaries, while late gadolinium enhancement and T2-weighted CMR sequences visualize myocardial scar and edema of MI, respectively. Existing methods usually fuse anatomical and pathological information from different CMR sequences for MyoPS, but assume that these images have been spatially aligned. However, MS-CMR images are usually unaligned due to the respiratory motions in clinical practices, which poses additional challenges for MyoPS. This work presents an automatic MyoPS framework for unaligned MS-CMR images. Specifically, we design a combined computing model for simultaneous image registration and information fusion, which aggregates multi-sequence features into a common space to extract anatomical structures (i.e., myocardium). Consequently, we can highlight the informative regions in the common space via the extracted myocardium to improve MyoPS performance, considering the spatial relationship between myocardial pathologies and myocardium. Experiments on a private MS-CMR dataset and a public dataset from the MYOPS2020 challenge show that our framework could achieve promising performance for fully automatic MyoPS.**

Index Terms— **Myocardial pathology, Multi-sequence cardiac magnetic resonance, Registration, Segmentation**

I. INTRODUCTION

Acute myocardial infarction (MI) is the most severe coronary artery disease, leading to more than a third of deaths in developed nations annually [1]. It could cause irreversible damage to the myocardium by acute ischemia [2]. Cardiac magnetic resonance (CMR) imaging, such as late gadolinium enhancement (LGE), has been established as the clinical standard for myocardial damage evaluation [3]. Delineating the damaged regions of myocardial muscles could assist MI risk stratification and treatment decision-making. However, manual delineation is extremely time-consuming due to the variation of shape, location and intensity of damaged regions. Automatic segmentation approaches therefore have attracted more research attention.

Conventional automatic methods, such as the signal threshold to reference mean [4], full-width at half-maximum [5], region growing [6] and graph-cuts [7], have been widely studied for myocardial infarcts (also known as "scars") segmentation. Recently, deep learning (DL) is widely employed to perform cardiac image analysis [8], [9]. Several works obtained promising accuracy via utilizing DL for myocardial pathology segmentation (MyoPS) from LGE images [10]–[12]. Besides, prior knowledge was employed to further improve DL methods. For instance, the location information of the left ventricle (LV) myocardium can significantly improve scar segmentation results due to the spatial relationship between scars and myocardium. Zabihollahy *et al.* proposed a scar segmentation method for LGE images, their method relied on the delineation of myocardium contours [12]. Note that automatically extracting myocardium from LGE images remains a challenge, due to the heterogeneous intensity distribution of myocardium [13]. Researchers thus developed a shape reconstruction mechanism [14] or model ensemble strategies [15], [16] to mitigate the affect of abnormal intensity.

In addition to mono-sequence (such as LGE) CMR images, researchers have developed methods to process multi-sequence CMR (MS-CMR) images. Clinically, MS-CMR images can provide various information about the heart [17]. For instance, balanced steady-state free precession (bSSFP) cine sequences present clear myocardium boundaries [see I_{bSSFP} in Fig. 1 (a)], T2-weighted (T2) CMR images provide incremental diagnostic and prognostic edema information for the scars of LGE CMR images [18] [see I_{LGE} and I_{T2} in Fig. 1 (a)]. Combining these MS-CMR images could provide relevant and complementary information for clinical analysis, which is critical for the diagnosis and treatment management of MI diseases [13], [19], [20]. Moreover, utilizing MS-CMR images could also potentially promote the performance of MyoPS methods. For instance, Fahmy *et al.* verified that adopting

W Ding and L Huang are with the College of Physics and Information Engineering, Fuzhou University, Fuzhou 350117, China (n191110003@fzu.edu.cn; hlq@fzu.edu.cn).

L Li is with the Department of Engineering Science, University of Oxford, Oxford, UK (e-mail: lei.li@eng.ox.ac.uk).

J Qiu, S Wang and X Zhuang are with the School of Data Science, Fudan University, Shanghai, China (qjy980811@gmail.com; 21110980009@m.fudan.edu.cn; zxh@fudan.edu.cn).

Y Chen and S Yang are with the Department of Radiology, Zhongshan Hospital, Fudan University and also the Department of Medical Imaging, Shanghai Medical School, Fudan University and Shanghai Institute of Medical Imaging, Shanghai 200032, China (chen.yinyin@zs-hospital.sh.cn; yang.shan@zs-hospital.sh.cn).

bSSFP could further improve the scar segmentation on LGE CMR images [21]. To fully explore the potential advantages of using MS-CMR images, Zhuang *et al.* first organized MYOPS2020 challenge[1] for the design of MyoPS methods [22].

A common limitation of current DL-based MyoPS methods is that they only can process pre-aligned MS-CMR images [21], [23], [24]. Meanwhile, the only available public MS-CMR dataset (MYOPS2020 challenge dataset) for MyoPS has been pre-aligned prior to release. In clinical applications, there may exist misalignment among MS-CMR images due to respiratory motions [see Fig. 1 (a) and (c)]. For unaligned MS-CMR images, the spatial relationship of anatomy and pathology regions protruded by different CMR images, could not be maintained consistently. Therefore, integrating information from different CMR images into a common space is desired, which could facilitate the monitoring [see Fig. 1 (a) and (d)] and diagnosis of MI diseases [18].
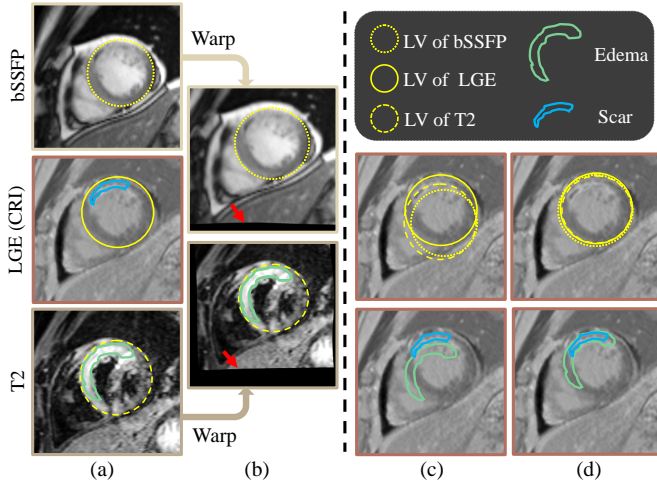
Fig. 1: Visualization of unaligned and aligned multi-sequence cardiac magnetic resonance (MS-CMR) images. (a) Short-axis views of unaligned MS-CMR images, i.e., bSSFP (top), LGE (middle) and T2 (bottom), with contours of the left ventricle (LV) epicardium, scar and edema regions. (b) Warped bSSFP and T2 images with contours of the LV epicardium and edema regions. Here, bSSFP and T2 images are registered to LGE via our proposed method. One can follow red arrows to observe the differences between original and warped images. (c) Stack of the label contours of unaligned CMR images. (d) Stack of the label contours of aligned CMR images. In sub-figure (c) and (d), we overlay the LV epicardium and myocardial pathology (scars and edema) contours from different CMR images on LGE. One can that observe LV epicardium contours of original source images are initially misaligned [see (c)], and become aligned after registering [see (d)]. CRI (common reference image) indicates the selected reference image for multi-sequence registration.

This work aims to perform MyoPS for unaligned MS-CMR images from practical clinics, which segments scar,

[1] http://www.sdspeople.fudan.edu.cn/zhuangxiahai/0/myops20/

edema and healthy myocardium within one unified result for each patient. We present a combined computing framework, referred to as U-MyoPS, for MyoPS [13]. U-MyoPS achieves MS-CMR image registration and myocardial segmentation and MyoPS in a unified DL-based schema. Specifically, we propose a multi-sequence fusion (MSF) block with a TPS model to fuse unaligned MS-CMR information for myocardial segmentation. We also fuse unaligned pathology information based on TPS registration in U-MyoPS, facilitating pathology segmentation. Moreover, we introduce a spatial prior gate (SPG) to propagate myocardium information to promote the performance of pathology segmentation.

II. METHOD

Fig. 2 shows the pipeline of U-MyoPS, which is a combined computing method to segment myocardial pathologies from MS-CMR images while align them simultaneously. Initially, the input bSSFP, T2 and LGE CMR images are registered into a common space (Section II-A). Then, an anatomical structure where pathologies may exist is extracted as the spatial prior (Section II-B). Finally, U-MyoPS segments myocardial pathology regions inside the spatial prior (Section II-C).

A. MS-CMR Image Registration

We align MS-CMR images into a common space via neural networks. Let $\mathcal{I} = \{I_{bSSFP}, I_{LGE}, I_{T2}\}$ denotes a set of 2D MS-CMR images extracted from the CMR data of the same subject (see Section III-A for extraction process). The size of each extracted image is $H \times W$. To align these images, we can set one of them as the common reference image (CRI), and register the rest images to it. For convenience, we set I_{LGE} as the CRI in this section. In U-MyoPS, we introduce three encoders (E_{bSSFP}, E_{LGE} and E_{T2}) to capture underlying structural information from $\mathcal{I}$, and two registration heads (R_{bSSFP} and R_{T2}) to estimate TPS transformations for registration.

A TPS transformation is parameterized via a grid of control points [25]. Briefly, we set an imaginary grid of control points on I_{bSSFP} and I_{T2}, and warp the images according to the displacements of control points. In U-MyoPS, the grid is defined with $m \times m$ equally spaced control points. R_{bSSFP} and R_{T2} predict the displacements of each control point:

$$\mathcal{G}_{bSSFP} = \{(\delta x_k^{bSSFP}, \delta y_k^{bSSFP}) | k = 1...m \times m\},$$
$$\mathcal{G}_{T2} = \{(\delta x_k^{T2}, \delta y_k^{T2}) | k = 1...m \times m\}, \quad (1)$$

where $(\delta x_k^{bSSFP}, \delta y_k^{bSSFP})$ and $(\delta x_k^{T2}, \delta y_k^{T2})$ are the displacements of control point (x_k, y_k). I_{bSSFP} and I_{T2} can be warped to I_{LGE} by the predicted displacements as follows:

$$\tilde{I}_{bSSFP} = \mathcal{T}_{\mathcal{G}_{bSSFP}}(I_{bSSFP}),$$
$$\tilde{I}_{T2} = \mathcal{T}_{\mathcal{G}_{T2}}(I_{T2}), \quad (2)$$

where $\tilde{I}_{bSSFP}$ and $\tilde{I}_{T2}$ are the warped images, $\mathcal{T}_{\mathcal{G}_{bSSFP}}$ and $\mathcal{T}_{\mathcal{G}_{T2}}$ denote the mapping function, whose parameters were determined by $\mathcal{G}_{bSSFP}$ and $\mathcal{G}_{T2}$ via existing DL-based closed-form solution [26], [27], respectively. After registration, we can compensate the misalignment of $\mathcal{I}$, and obtain aligned
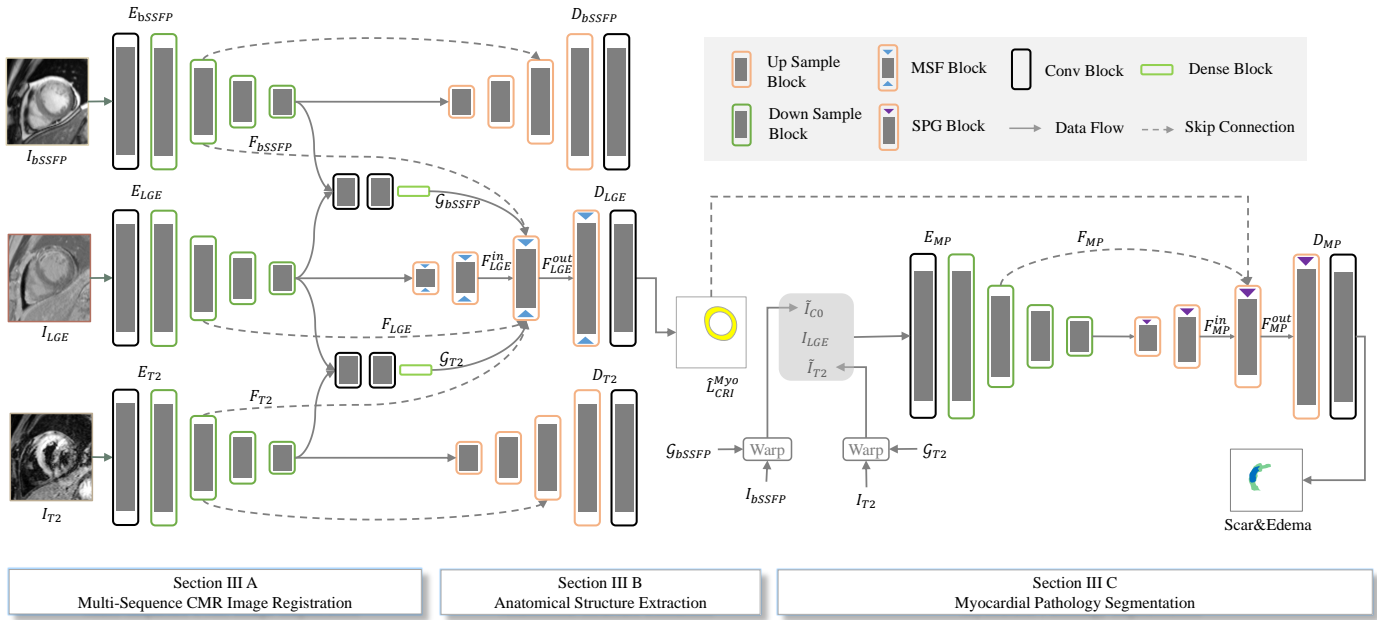
Fig. 2: Pipeline of the myocardial pathology segmentation (MyoPS) framework, referred to as U-MyoPS, for unaligned multi-sequence cardiac magnetic resonance (MS-CMR) images. The network architecture of the U-MyoPS includes three encoders (E_{bSSFP}, E_{LGE} and E_{T2}) and two registration heads (R_{bSSFP} and R_{T2}) for MS-CMR registration, three decoders (D_{bSSFP}, D_{LGE} and D_{T2}) for MS-CMR anatomical structure extraction, and a prior-aware network (E_{MP} and D_{MP}) for MyoPS. Note that we only retain representative connections between encoders (E_{bSSFP}, E_{LGE}, E_{T2} and E_{MP}) and decoders (D_{bSSFP}, D_{LGE}, D_{T2} and D_{MP}), and omit the rest ones for better visualization. This figure illustrates when U-MyoPS takes three CMR images $\mathcal{I} = \{I_{bSSFP}, I_{LGE}, I_{T2}\}$ as input, and sets I_{LGE} as the common reference image (CRI) for registration and MyoPS.

MS-CMR images $\mathcal{I}' = \{\tilde{I}_{bSSFP}, I_{LGE}, \tilde{I}_{T2}\}$ in the common space. Consequently, the spatial relationship of anatomy and pathology regions protruded by different CMR images could be consistent in $\mathcal{I}'$, promoting the subsequent anatomical structure extraction and pathology segmentation tasks.

Registration Loss: To optimize the parameters of the encoders and registration heads, we introduce a multi-sequence registration loss function as follows:

$$\mathcal{L}oss_{Reg} = - \sum_{j \in \{bSSFP, T2\}} \mathcal{D}ice(\mathcal{T}_{\mathcal{G}_j}(L_j^{ana}), L_{LGE}^{ana}), \quad (3)$$

where $\mathcal{D}ice(a, b)$ calculates the Dice score between label a and b [28], L_j^{ana} and L_{LGE}^{ana} denote the corresponding anatomical structure labels, i.e., myocardium, LV and right ventricle (RV), of MS-CMR images. With the supervision of $\mathcal{L}oss_{Reg}$, registration headers could learn to align MS-CMR images.

B. Anatomical Structure Extraction

We introduce a decoder D_{LGE} to extract the anatomical structure, i.e., myocardium, of CRIs. Generally, D_{LGE} could utilize feature maps from E_{LGE} to predict myocardium regions. Note that the feature maps from E_{bSSFP} and E_{T2} also provide myocardium structure information, we further propose MSF to fuse these information into D_{LGE} to improve myocardium extraction.

Fig. 3 visualizes MSF block. The main idea of MSF lies in compensating spatial misalignment before feature map
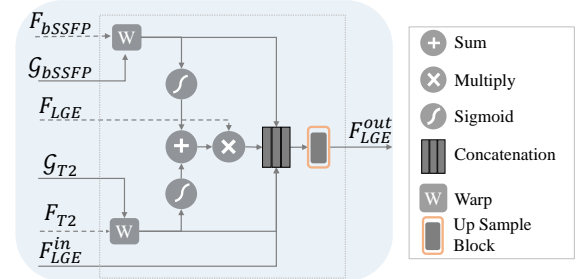
Fig. 3: Schematic illustration of proposed multi-sequence fusion (MSF) block in D_{LGE}.

fusion. Let F_{LGE}^{in} be the previous output in D_{LGE}, while F_{bSSFP}, F_{T2} and F_{LGE} be the feature maps at i-th level of E_{bSSFP}, E_{T2} and E_{LGE}, respectively. Since I_{bSSFP}, I_{T2} and I_{LGE} were unaligned images, the corresponding feature maps F_{bSSFP}, F_{T2} and I_{LGE} remained unaligned until input into MSF module. Thus, F_{bSSFP} and F_{T2} could not be directly fused with F_{LGE}. Here, we employ TPS transformations to re-calibrate the feature maps for fusion. Note that the spatial sizes of feature maps vary across different levels of encoders due to down-sample operations (i.e., max pooling). To transform the feature maps, we first adjust TPS parameters as follows:

$$\mathcal{G}_{bSSFP}^{h \times w} = \{(\delta x_k^{bSSFP} \times h/H, \delta y_k^{bSSFP} \times w/W) | k = 1...m \times m\},$$
$$\mathcal{G}_{T2}^{h \times w} = \{(\delta x_k^{T2} \times h/H, \delta y_k^{T2} \times w/W) | k = 1...m \times m\},$$
$$(4)$$

where $h \times w$ and $H \times W$ denote the spatial size of feature maps and original CMR images, respectively. Then, F_{bSSFP} and F_{T2} can be warped via $\mathcal{G}_{bSSFP}^{h \times w}$ and $\mathcal{G}_{T2}^{h \times w}$, respectively (see (2)). Finally, we concatenate the warped F_{bSSFP} and F_{T2} together with F_{LGE} and F_{LGE}^{in}. The output of MSF F_{LGE}^{out} contains myocardium information from MS-CMR images, which could improve the extraction of myocardium structures.

Myocardium Extraction Loss: The extracted myocardium structure should be consistent with the myocardium contour of CRI images. To optimize the parameter of D_{LGE}, we introduce a myocardium extraction loss as follows:

$$\mathcal{L}oss_{Myo} = -\mathcal{D}ice(\hat{L}_{LGE}^{Myo}, L_{LGE}^{Myo}), \quad (5)$$

where $\hat{L}_{LGE}^{Myo}$ and L_{LGE}^{Myo} are the extracted myocardium and gold standard myocardium label of I_{LGE} (CRI). Besides, we introduce two additional decoders D_{bSSFP} and D_{T2} to capture myocardial information from I_{bSSFP} and I_{T2}, respectively. D_{bSSFP} and D_{T2} are trained via myocardium constraint loss as follows:

$$\mathcal{L}oss_{Cons} = -\sum_{j \in \{bSSFP,T2\}} \mathcal{D}ice(\hat{L}_{j}^{Myo}, L_{j}^{Myo}), \quad (6)$$

where $\hat{L}_{j}^{Myo}$ and L_{j}^{Myo} are the predicted myocardium and gold standard labels of CMR images, respectively. With the constraint loss, E_{bSSFP} and E_{T2} could focus on capturing myocardial features from I_{bSSFP} and I_{T2}, facilitating the myocardium extraction of D_{LGE}.

Furthermore, we simultaneously train anatomical structure extraction with multi-sequence registration tasks via a hybrid loss function:

$$\mathcal{L}oss_{Hyb} = \mathcal{L}oss_{Reg} + \lambda(\mathcal{L}oss_{Cons} + \mathcal{L}oss_{Myo}), \quad (7)$$

where λ is the balance coefficient for multi-sequence registration, myocardium extraction and myocardium constraint losses. Here, U-MyoPS performs MS-CMR image registration and myocardium segmentation simultaneously and collaboratively, and optimizes network parameters by merging loss functions, which is similar to existing joint optimization methods [29]–[31]. Nevertheless, U-MyoPS further introduces a novel network module, i.e., MSF, to promote joint optimization tasks.

C. Myocardial Pathology Segmentation

With extracted myocardium ($\hat{L}_{LGE}^{Myo}$), we construct a prior-aware sub-network to segment edema and scars from $\mathcal{I}'$. The backbone of the network is a U-Shape model [32], including an encoder (E_{MP}) and a decoder (D_{MP}). Notably, $\hat{L}_{LGE}^{Myo}$ provides spatial prior for myocardial pathologies. We propose SPG in D_{MP} to incorporate $\hat{L}_{LGE}^{Myo}$ for pathology segmentation.

Fig. 4 shows SPG block, which aims to propagate myocardium information to promote MyoPS. Let F_{MP}^{in} be previous output in D_{MP}, and F_{MP} denotes a feature map from i-th level of E_{MP}. SPG could highlight informative regions of F_{MP}, and aggregate the information of recalibrated F_{MP} and F_{MP}^{in} for pathology prediction. Specifically, we first add F_{MP} with F_{MP}^{in}, and highlight their informative region by
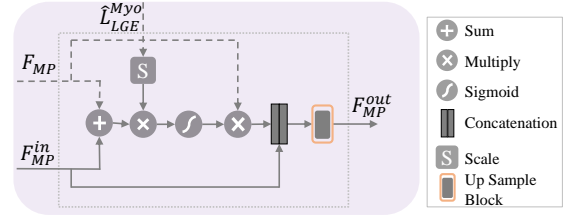

Fig. 4: Schematic illustration of the proposed spatial prior gate (SPG) block in D_{MP}

multiplying with $\hat{L}_{LGE}^{Myo}$. Note that the spatial sizes of F_{MP} and F_{MP}^{in} vary in different levels, and we thus employ a scale operation to adjust $\hat{L}_{LGE}^{Myo}$ to different sizes of F_{MP} and F_{MP}^{in}. After then, sigmoid operations are applied to obtain an attention map. Finally, we multiply F_{MP} with the attention map, and concatenate the multiplication result with F_{MP}^{in} to obtain the output of SPG F_{MP}^{out}.

Myocardial Pathology Segmentation Loss: We train the prior-aware sub-network by minimizing the difference between predicted and gold standard myocardial pathology labels:

$$\mathcal{L}oss_{MP} = -\mathcal{D}ice(\hat{L}', L') + \mathcal{C}E(\hat{L}', L'), \quad (8)$$

where $\hat{L}'$ and L' are the predicted and gold standard pathology labels of $\mathcal{I}'$, respectively; $\mathcal{C}E(a, b)$ calculates the cross-entropy between a and b. Note that scar and edema labels were only originally delineated in unaligned LGE and T2 images, respectively [see the lower part of Fig. 1 (c)]. We align the original scar and edema labels into a common space to obtain the gold standard pathology label of $\mathcal{I}'$. Namely, L' is a combination of scar and edema labels as shown in the lower part of Fig. 1 (d). For the overlap part of the scar and edema labels, we denote them as scar regions. For the non-overlapped parts, we retained to use the original label.

Finally, the overall parameters of U-MyoPS, i.e., E_{bSSFP}, E_{LGE}, E_{T2}, D_{bSSFP}, D_{LGE}, D_{T2}, R_{bSSFP}, R_{T2}, E_{MP} and D_{MP}, can be optimized by minimizing $\mathcal{L}oss_{Hyb}$ and $\mathcal{L}oss_{MP}$.

III. Experiments

A. Datasets and Experiment Settings

We evaluated the proposed framework, i.e., U-MyoPS, on a private unaligned MS-CMR dataset (pMM-CMR dataset) and a public pre-aligned MS-CMR dataset (MYOPS2020 challenge dataset).

- pMM-CMR dataset: This dataset includes 50 unaligned MS-CMR (i.e., bSSFP, LGE and T2) images. The typical imaging parameters of bSSFP were as follows: field of view (FOV) = $283 \sim 453 \times 283 \sim 453$ mm^2, pixel size= $1.47 \sim 2.36 \times 1.47 \sim 2.36$ mm^2 , number of slices= $8 \sim 10$, slice thickness= 10 mm. The imaging parameters of LGE were: FOV = $283 \sim 453 \times 283 \sim 453$ mm^2, pixel size = $1.33 \sim 1.86 \times 1.33 \sim 1.86$ mm^2, number of slices= $4 \sim 11$, and slice thickness = 10 mm. The imaging parameters of T2 were as follows: FOV = $283 \sim 453 \times 283 \sim 453$ mm^2,

TABLE I: The demographic information of MYOPS2020 and pMM-CMR datasets. We randomly split the images of pMM-CMR to generate training and test set. No: number of images. M/ F: male/ female. MI: myocardial infarction.

| Dataset	No	Age	M/ F	Training/ Test	Diagnoisis
MYOPS2020	45	56.2 ± 7.92	45M/ 0F	20/ 25	acute MI
pMM-CMR	50	55.6 ± 8.69	48M/ 2F	20/ 30	acute MI

pixel size = $1.11{\sim}1.77 \times 1.11{\sim}1.77$ mm^2, number of slice= $2{\sim}10$, and slices thickness = 10 mm.

We employed the end-diastolic cardiac phase of bSSFP cine data, which is consistent to the cardiac phase of LGE and T2. The ground truth contours were annotated by one cardiologist. The delineation was performed by slice-wise using ITK-SNAP software [33]. For each slice, the cardiologist acquired labels as follows: (1) The cardiologist delineated the structure labels, i.e., LV, RV and myocardium. (2) The cardiologist manually adjusted gray-scale to identify all highlighted areas within the myocardium as scars in LGE images [21]. If necessary, the cardiologist manual included scars that were not identified by the intensity threshold (such as microvascular obstruction) [21]. (3) The cardiologist manually adjusted gray-scale to identify all highlighted areas within the myocardium as edema in T2 images. If necessary, the cardiologist manual excluded areas representing noise or artefacts (such as suppressed blood signal) [34]. In experiments, we randomly selected 20 unaligned MS-CMR images for network training and validation, while leaved the rest 30 for testing.

- MYOPS2020 challenge dataset: This dataset contains 45 (25 labeled and 20 unlabeled) MS-CMR (i.e., bSSFP, LGE and T2) images [20]. All released images have been aligned into a common space via MvMM [13]. Similar to pMM-CMR dataset, the labeled CMR images were manually delineated with scar, edema, myocardium, LV and RV labels. In experiments, we used the labeled images for network training and validation, and tested our method on unlabeled images with MYOPS2020 evaluation kit[2].

pMM-CMR and MYOPS2020 dataset are independent datasets from different clinical centers. Table I lists the demographic information of two datasets. The original CMR images of the two datasets are breath-hold multi-slice 2D images, acquired along the cardiac short-views. We extracted slices from the original images of the same subject for network training and testing. Fig. 5 illustrates the extraction procedure. Given bSSFP, T2 and LGE images of the same subjects (see the top row of Fig. 5), we first pre-aligned these CMR images via rigid transformation. Note that the field-of-views may vary across different sequences. For example, bSSFP usually visualizes the whole LV, while T2 may only cover the sub-region of LV. We then employed the slices from the physical regions that were simultaneously imaged by bSSFP, T2 and LGE (see the middle row of Fig. 5). After then,

by regarding LGE slice (I_{LGE}) as the common reference image, we extracted the corresponding bSSFP (I_{bSSFP}) and T2 (I_{T2}) slices which have the closest physical distance to it (see the bottom row of Fig. 5). Note that to calculate the physical distance between CMR slices, we directly employed the transformation parameters of the images from the header of NIFIT data [35]. Finally, all slices were cropped by centering at the heart regions. Each extracted slice was re-sampled with the same spatial resolution, and normalized via Z-score. *We primarily evaluated on the pMM-CMR dataset (see Sec. III-D, III-E,III-F, III-H and III-G), while the MYOPS2020 challenge dataset was only used for a comparison with the state-of-the-art methods on a public dataset (see Sec. III-I).*
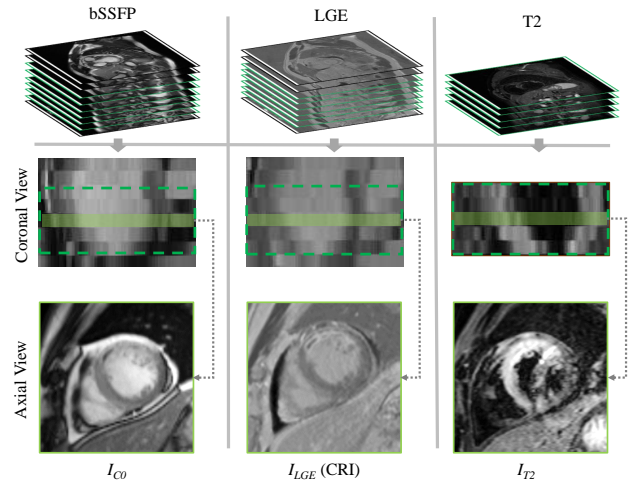
Fig. 5: Illustration of multi-sequence cardiac magnetic resonance image extraction. Green dashed rectangles mark the physical regions that are simultaneously imaged by bSSFP, T2 and LGE. CRI (common reference image) indicates the selected reference image for multi-sequence registration.

B. Network Training

U-MyoPS was implemented by Pytorch and trained with Adam optimizer[3]. For MS-CMR image registration, TPS grids were initially set with 4×4 equally-spaced control points:

$$\mathcal{G}_C = \{(x_k, y_k)|k=1,\ldots,16\}, \tag{9}$$

where $x_k, y_k \in \{p|p = 256 \times (-0.98 + 0.65 \times n), n = 0,1,2,3\}$. Note that we set the center of images to (0,0), and resized images to $256{\times}256$ when performing TPS transformation. To train U-MyoPS, unaligned MS-CMR images were fed into the network. We first jointly trained the multi-sequence registration and anatomical structure extraction with the hybrid loss [see (7)] by setting λ to 0.1. After converging, we froze the parameters for multi-sequence registration and anatomical structure extraction, and then optimized the parameters of prior-aware sub-network by minimizing pathology segmentation loss [see (8)].

C. Gold Standard and Evaluation Metrics

We evaluated the accuracies of MyoPS in the common space. Note that in the final MyoPS visualization, edema labels were partially overlapped by scar labels in common spaces. We refer to the union of scar and edema labels as edema in the following evaluation and visualization [20]. Here, Dice and Hausdorff distance (HD) and statistical measurements [i.e., Sensitivity (Sen) and Precision (Pre)] were employed for MyoPS evaluation. Meanwhile, scar size, scar transmurality and edema size were included for clinical quantification. Besides, Dice and HD between the warped source and target labels were adopted for multi-sequence registration evaluation.

D. Results of MyoPS on pMM-CMR Dataset

1) Comparison with Semantic Segmentation Methods: We first compared U-MyoPS with existing DL-based semantic segmentation methods. Here, we implemented five semantic segmentation based on their official codes[4] as well as our method:

- nn-Unet^{Una}: nn-Unet [36] which took unaligned MS-CMR images as inputs, and predicted scarring and edema regions. Note that the predicted scarring and edema regions were unaligned due to the misalignment among input images.
- PSN$_{LGE}$: U-shape [32] pathology segmentation network which was trained with I_{LGE} as well as corresponding scar labels.
- PSN$_{T2}$: U-shape [32] pathology segmentation network which was trained with I_{T2} as well as corresponding edema labels.
- MvMM+nn-Unet: nn-Unet [36] which took aligned MS-CMR images as inputs, and predicted scarring and edema regions. Here, the MS-CMR images were aligned by MvMM [13], which was also the standard tool for aligning MS-CMR images of MYOPS2020 challenge dataset [20].
- MvMM+AWSnet: AWSnet [23] which took aligned MS-CMR images as inputs, and predicted scarring and edema regions. Here, MS-CMR images were also aligned by MvMM [13]. AWSnet is a promising coarse-to-fine MyoPS method. It first obtained LV regions from bSSFP images. Then, it segmented scars and edema based on the LV regions.
- U-MyoPS$_{bLT}$: U-MyoPS which utilizes unaligned MS-CMR images for scar and edema segmentation.

The upper part of Table II lists MyoPS results of different methods on pMM-CMR. MvMM+nn-Unet obtained better scar ($p < 0.01$) and edema ($p < 0.05$) results against nn-Unet^{Una}. The reason is that MvMM+nn-Unet utilized aligned MS-CMR images, and the pathological and anatomical information from the aligned images could complement each other for segmentation. Meanwhile, U-MyoPS$_{bTL}$ achieved better results

than nn-Unet^{Una} for all evaluation metrics. One of the reasons is that U-MyoPS$_{bTL}$ aligned MS-CMR for segmentation.

U-MyoPS$_{bLT}$ obtained better scar and edema results against mono-sequence semantic segmentation methods (i.e., PSN$_{LGE}$ and PSN$_{T2}$) which only utilized single sequence (LGE or T2) of CMR images. Particularly, for scar segmentation, U-MyoPS$_{bTL}$ improved Dice and HD by 8.92% ($p < 0.01$) and 13.84 mm ($p < 0.01$) against PSN$_{LGE}$. Meanwhile, compared to PSN$_{T2}$, U-MyoPS$_{bTL}$ obtained better Dice (8.20%, $p < 0.01$) and HD (3.19 mm, $p = 0.21$) results for edema segmentation. This is because U-MyoPS$_{bLT}$ aligned MS-CMR images for MyoPS. Segmentation methods could obtain more robust pixel-wise classification based on the intensity information from aligned scarring and edema regions.

U-MyoPS$_{bLT}$ achieved better performance than the semantic segmentation method (i.e., MvMM+nn-Unet and MvMM+AWSnet) which consumed pre-aligned MS-CMR images. One can see U-MyoPS$_{bLT}$ outperformed MvMM+nn-Unet for scar ($p < 0.01$) and edema ($p < 0.01$) segmentation results in terms of Dice and HD. The underlying reason was that U-MyoPS$_{bLT}$ extracted myocardium as spatial prior, facilitating the subsequent MyoPS performance. Meanwhile, U-MyoPS$_{bLT}$ obtained comparable results to MvMM+AWSnet on scar ($p = 0.24$) and edema ($p = 0.17$) segmentation in terms of Dice. Nevertheless, U-MyoPS$_{bLT}$ was computationally efficient. The average runtime of MvMM+AWSnet was about 469 seconds (MvMM: 461 seconds; AWSnet: 8 seconds), whereas U-MyoPS$_{bLT}$ only required about 10 seconds to segment pathologies from the unaligned MS-CMR images of a subject.

Furthermore, we conducted an inter-observer variations study for MyoPS based on Dice metric. The inter-observer variations were 70.4% and 77.9% for scar and edema segmentation in terms of Dice, respectively. As listed in Table II, U-MyoPS$_{bLT}$ obtained 64.9% and 76.0% for scar and edema segmentation, respectively. U-MyoPS$_{bLT}$ was worse than the inter-observer for scar segmentation, but close for edema segmentation.

Fig. 6 visualizes the MyoPS results of different methods. Here, the gold standard pathology labels were the ones of U-MyoPS$_{bLT}$[5]. As indicated by the red Arrows, U-MyoPS$_{bLT}$ reduced inappropriate segmentation, and mitigated outliers against comparison methods. This demonstrated the promising of U-MyoPS$_{bLT}$.

2) Ablation Study of MSF and SPG: We implemented two variants of U-MyoPS$_{bLT}$ for the ablation study of MSF and SPG:

- U-MyoPS$_{bLT}^{w/o\ MSF}$: Our U-MyoPS$_{bLT}$ model without using MSF.
- U-MyoPS$_{bLT}^{w/o\ SPG}$: Our U-MyoPS$_{bLT}$ model without using SPG.

The lower part of Table II presents the result of U-

---

[4] PSN: https://github.com/ShawnBIT/UNet-family;
nn-Unet: https://github.com/MIC-DKFZ/nnUNet;
MvMM: http://www.sdspeople.fudan.edu.cn/zhuangxiahai/0/zxhproj/;
AWSnet: https://github.com/soleilssss/AWSnet/tree/master.

[5] The scar and edema were manually delineated in original unaligned T2 and LGE images. U-MyoPS and MvMM+nn-Unet aligned these images into a common space, and performed MyoPS for the aligned images. Note that different methods may obtain different alignments of MS-CMR images. Thus, the corresponding gold standard pathology label may also differ slightly.

TABLE II: Performance of different MyoPS methods. Note that PSN_{LGE} and PSN_{T2} could only predict scar and edema of LGE and T2 images, respectively. Subscript "$_{bLT}$": bSSFP, LGE and T2 images. The best results are labeled in **bold**.

Method	Sequences			Scar				Edema			
	bSSFP	LGE	T2	Dice (%) ↑	Sen (%) ↑	Pre (%) ↑	HD (mm) ↓	Dice (%) ↑	Sen (%) ↑	Pre (%) ↑	HD (mm) ↓
nn-Unet^{Una}	✓	✓	✓	44.16 (17.47)	46.68 (20.30)	44.05 (18.11)	37.88 (21.84)	66.48 (14.74)	70.97 (13.26)	64.81 (18.47)	38.28 (23.40)
PSN_{LGE}	×	✓	×	55.99 (17.52)	61.66 (20.21)	53.25 (18.80)	43.01 (23.08)	N/A			
PSN_{T2}	×	×	✓	N/A				67.82 (19.01)	79.42 (12.86)	61.97 (22.94)	31.07 (23.79)
MvMM+nn-Unet	✓	✓	✓	57.18 (11.18)	62.29 (12.59)	54.23 (13.31)	36.93 (17.50)	69.87 (14.13)	78.42 (12.66)	65.25 (17.96)	37.79 (22.29)
MvMM+AWSnet	✓	✓	✓	62.38 (14.47)	68.02 (18.28)	59.20 (13.52)	36.56 (15.53)	74.23 (12.87)	**82.13 (8.875)**	70.03 (17.79)	30.12 (22.97)
U-MyoPS$_{bLT}$	✓	✓	✓	**64.92 (9.816)**	**68.30 (12.56)**	63.34 (11.71)	**29.16 (16.65)**	**76.01 (9.784)**	80.49 (8.942)	**73.53 (14.05)**	**27.89 (18.45)**
U-MyoPS$_{bLT}^{w/o\ MSF}$	✓	✓	✓	64.58 (9.762)	64.76 (12.08)	**66.12 (11.77)**	33.61 (18.21)	75.15 (11.21)	79.78 (10.56)	72.56 (14.88)	32.65 (21.38)
U-MyoPS$_{bLT}^{w/o\ SPG}$	✓	✓	✓	60.61 (10.11)	65.03 (14.21)	58.71 (12.36)	34.17 (19.32)	71.69 (13.56)	75.06 (11.97)	70.94 (18.38)	32.98 (19.61)
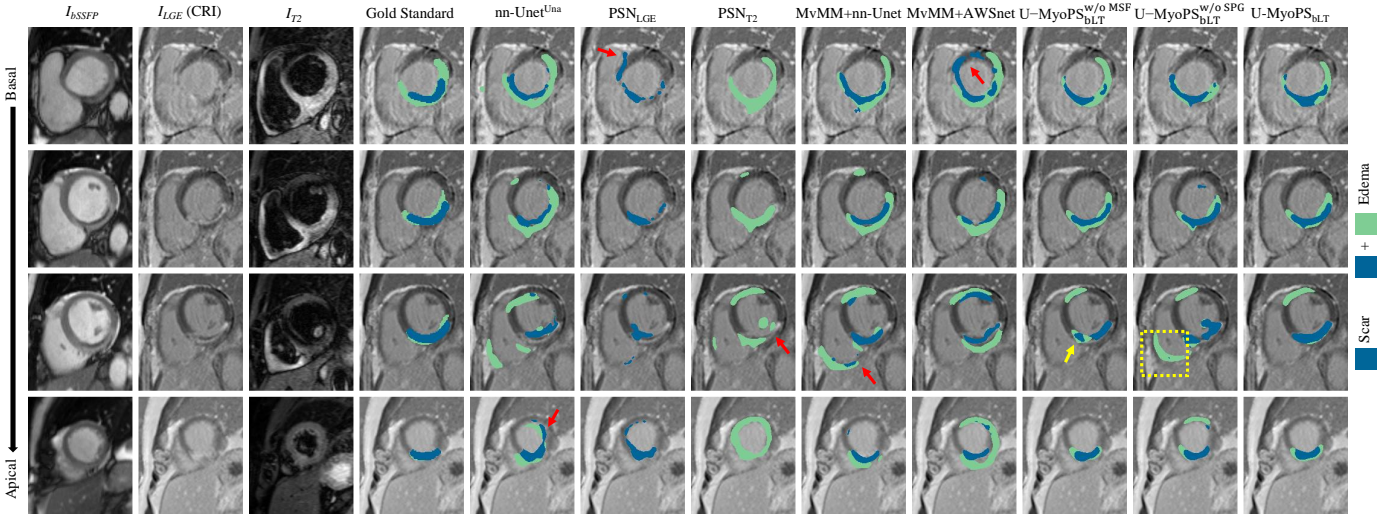
Fig. 6: Visualization of MyoPS results from basal to apical slices. The results are overlaid on the LGE images. The scarring and edema regions are colorized with blue and green, respectively. Arrows, circles and rectangles mark the typical regions where U-MyoPS$_{bLT}$ achieved better results. CRI (common reference image) indicates the selected reference image for multi-sequence registration.

MyoPS$_{bLT}^{w/o\ MSF}$. With MSF, U-MyoPS$_{bLT}$ achieved slight better scar ($p = 0.77$) and edema ($p = 0.24$) results to U-MyoPS$_{bLT}^{w/o\ MSF}$ in term of Dice. Notably, as MSF was also proposed to improve the myocardium structure extraction for MyoPS, one can refer to Section III-F.2 for the ablation study of MSF on myocardium structure extraction.

Meanwhile, the lower part of Table II presents the result of U-MyoPS$_{bLT}^{w/o\ SPG}$. Without SPG, U-MyoPS$_{bLT}^{w/o\ SPG}$ suffered performance degradation. For instance, compared to U-MyoPS$_{bLT}$, U-MyoPS$_{bLT}^{w/o\ SPG}$ decreased Sen by almost 4% ($p < 0.05$) and 5% ($p = 0.01$) for scar and edema segmentation, respectively. This is because the scarring and edema regions are in hlymyocardium. It would turn out to be harder for U-MyoPS$_{bLT}^{w/o\ SPG}$ to find more pathology regions without myocardium prior information.

Fig. 6 visualizes the MyoPS results of U-MyoPS$_{bLT}^{w/o\ MSF}$ and U-MyoPS$_{bLT}^{w/o\ SPG}$. Even U-MyoPS$_{bLT}^{w/o\ MSF}$ obtained comparable quantity results to U-MyoPS$_{bLT}$, U-MyoPS$_{bLT}$ still achieved more reasonable details (see yellow Arrows). The underlying reason is that U-MyoPS$_{bLT}$ obtained more plausible myocardium structures by using MSF (see Section III-F.2), which facilities segmentation details. Moreover, by using SPG, U-MyoPS$_{bLT}$ could reduce outliers (see yellow Rectangles) compared to U-MyoPS$_{bLT}^{w/o\ SPG}$. This indicated the benefit of employing spatial prior information for MyoPS.
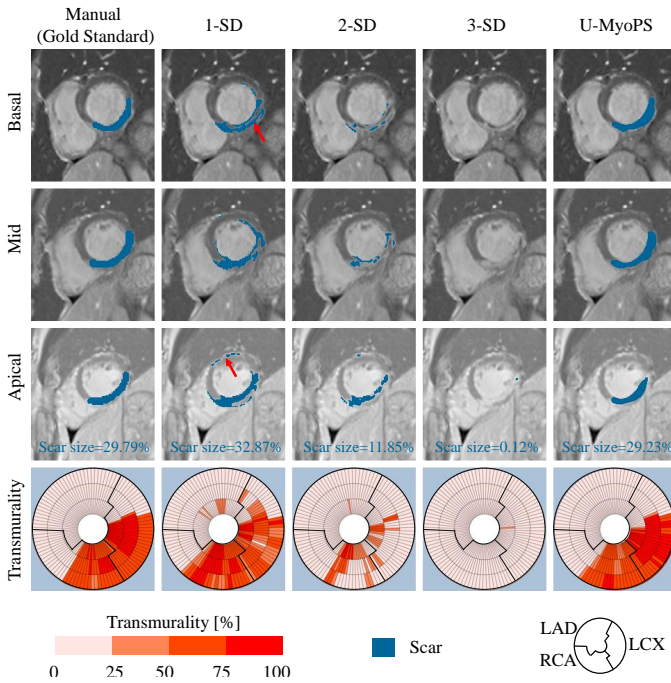
E. Results of Clinical Quantification

We evaluated the performance of U-MyoPS based on clinical indices, and compared U-MyoPS to clinical segmentation methods, namely 1-SD, 2-SD and 3-SD [37].

1) Results of scar size and transmurality: We employed two clinical indices, i.e., scar size and transmurality, for scar quantification. Scar size was quantified as the percentage of LV myocardium. For transmurality, we adopted centerline chord method [38], [39] to divide LV myocardium into 100 equally spaced chords. The transmurality of each chord was quantified as (scar pixels / chord pixels)×100%.

Fig. 7 shows a typical scar on left circumflex territory. 1-SD and U-MyoPS obtained closely matching results (scar size and transmurality) to the manual delineation. Whereas, 2-SD and 3-SD suffered under-segmentation, resulting in inaccuracy for measurements. Moreover, n-SD methods are sensitive to noises, while U-MyoPS could generate more clear and plausible results as indicated by arrows.

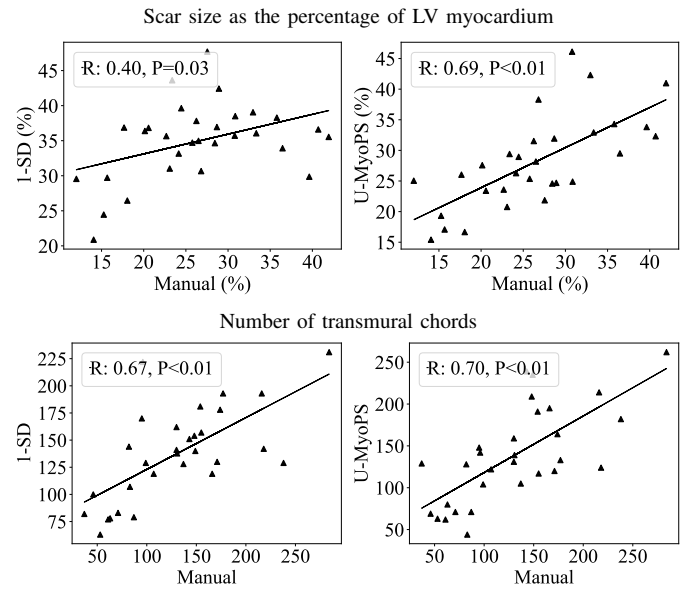Furthermore, we investigated the correlation among the

quantification results of 1-SD[6], U-MyoPS and manual delineation for each patient. Compared to 1-SD, U-MyoPS obtained slightly better results for scar size quantification, and achieved comparable performance for transmural chord quantification as shown in Fig. 8. Meanwhile, U-MyoPS showed significant correlations with manual delineation, the Pearson correlation coefficients were 0.69 ($p < 0.01$) and 0.70 ($p < 0.01$) for scar size and transmural chord, respectively. This supported that U-MyoPS could achieve robust performance for scar quantification.

Fig. 8: Assessment of transmurality and scar size of different methods. Here, we investigated the correlation between automatic methods (i.e., 1-SD and U-MyoPS) and manual delineation. We quantified the transmurality of patients by counting the number of transmural chords (transmurality $>$ 50%) based on centerline chord method [38], [39]. The top and bottom rows are correlation plots of scar size and transmurality quantification among different methods, respectively. R: Pearson correlation coefficients.

Fig. 7: Examples of myocardial scar size and transmurality. The scar sizes as the percentage of LV myocardium are in the apical slices. The transmurality of each subject is demonstrated in the bull-eyes plots of the last low. Each chord was encoded with different color according to its transmurality, i.e., misty-rose (viable): $0 \sim 25\%$; coral (likely viable): $26\% \sim 50\%$; orange red (likely nonviable) $51\% \sim 75\%$; red (nonviable): $76\% \sim 100\%$ [39]. Arrows indicate the regions where U-MyoPS achieved better results than 1-SD. LAD: left anterior descending artery; LCX: left circumflex artery; RCA: right coronary artery

F. Effects of the Number of Sequences

U-MyoPS aligned MS-CMR images for MyoPS. Since each of the sequences could provide different information, the myocardium and pathology segmentation could be improved by fusing more sequences. We further evaluated the effects of aligning different numbers of sequences on pMM-CMR dataset.
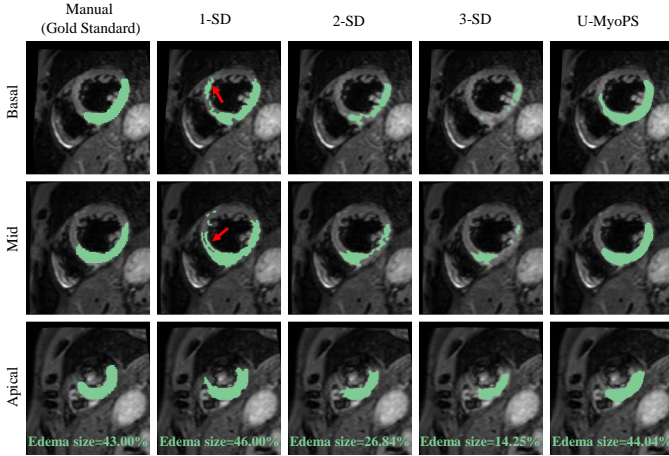
1) MyoPS vs. Number of Sequences: We first investigated the performance of U-MyoPS with different numbers of sequences. Here, we implemented additional two variants of U-MyoPS with different numbers of sequences:

- U-MyoPS$_{bL}$: U-MyoPS which utilized $\{I_{bSSFP}, I_{LGE}\}$ images for *scar* segmentation.
- U-MyoPS$_{LT}$: U-MyoPS which utilized $\{I_{LGE}, I_{T2}\}$ images for *scar and edema* segmentation.

Table III lists the MyoPS performance of U-MyoPS framework with different numbers of CMR sequences. U-MyoPS was capable of processing CMR images with different numbers (two or three) of sequences. Generally, the method using three sequences, i.e., U-MyoPS$_{bLT}$, achieved the best results in most metrics. Even the method using two sequences, i.e., U-MyoPS$_{LT}$, obtained best Pre of scar, the difference ($p = 0.56$) was not obvious when compared to U-MyoPS$_{bLT}$. Moreover, U-MyoPS$_{bLT}$ increased the Sen of scars by about 6% ($p < 0.01$) and 3% ($p = 0.05$) with additional sequence images when compared to U-MyoPS$_{LT}$ and U-MyoPS$_{bL}$, respectively. This implied the potential advantages of aligning more se-

2) Results of edema size: We quantified edema size as the percentage of LV myocardium. Fig. 9 visualizes a typical edema. Both 1-SD and U-MyoPS obtained better segmentation results than 2-SD and 3-SD. Notably, U-MyoPS could obtain more robust results against 1-SD as indicated by arrows. In Fig. 10, we further investigated the correlation among 1-SD, U-MyoPS and manual delineation. U-MyoPS obtained worse Pearson correlation coefficients (0.80 vs. 0.68) against 1-SD. Nevertheless, U-MyoPS achieved a significant ($p < 0.01$) correlation to manual delineation.

---

[6] Note that 1-SD obtained optimal performance against 2-SD and 3-SD in pMM-CMR dataset, we thus only employed 1-SD methods for correlation study.

TABLE III: Performance of U-MyoPS with different numbers of CMR sequence images. Subscript "$_{bL}$": bSSFP and LGE images; Subscript "$_{LT}$": LGE and T2 images; Subscript "$_{bLT}$": bSSFP, LGE and T2 images. NoS: Number of sequences. The best results are labeled in **bold**.

Method	Sequences				Scar				Edema			
	bSSFP	LGE	T2	NoS	Dice (%) ↑	Sen (%) ↑	Pre (%) ↑	HD (mm) ↓	Dice (%) ↑	Sen (%) ↑	Pre (%) ↑	HD (mm) ↓
U-MyoPS$_{bL}$	✓	✓	✗	2	61.72 (11.48)	63.95 (13.65)	60.85 (12.31)	35.26 (16.63)		N/A		
U-MyoPS$_{LT}$	✗	✓	✓	2	62.32 (10.58)	61.56 (12.26)	**64.61 (12.21)**	30.44 (17.58)	74.80 (12.29)	79.86 (10.62)	71.48 (15.47)	29.18 (20.17)
U-MyoPS$_{bLT}$	✓	✓	✓	3	**64.92 (9.816)**	**68.30 (12.56)**	63.34 (11.71)	**29.16 (16.65)**	**76.01 (9.784)**	**80.49 (8.942)**	**73.53 (14.05)**	**27.89 (18.45)**

Fig. 9: Examples of myocardial edema size. The edema sizes as the percentage of LV myocardium are in the apical slices. Arrows indicate the regions where U-MyoPS obtained better results than 1-SD
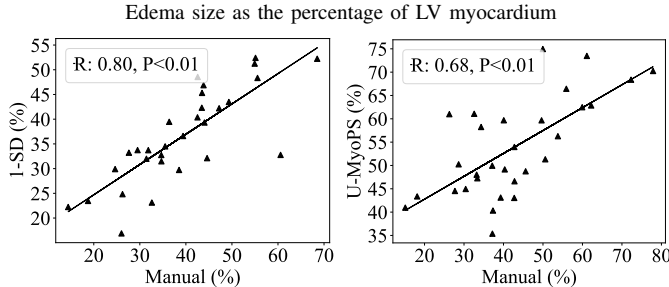
Fig. 10: Assessment of edema size of different methods. Here, we investigated the correlation between automatic methods (i.e., 1-SD and U-MyoPS) and manual delineation. R: Pearson correlation coefficients.

quences for MyoPS.

2) Myocardium Extraction vs. Number of Sequences: We investigated the performance of myocardium extraction with different numbers of sequences. Here, we presented three myocardium extraction methods with different numbers of sequences:

- Myo$_{bL}$ and Myo$_{LT}$: The anatomical structure extraction method of (see Section II-B) U-MyoPS which fused $\{I_{bSSFP}, I_{LGE}\}$ and $\{I_{LGE}, I_{T2}\}$ for myocardium extraction, respectively.
- Myo$_{bLT}$: The anatomical structure extraction method of U-MyoPS that fused $\{I_{bSSFP}, I_{LGE}, I_{T2}\}$ for my-

ocardium extraction.

Moreover, we implemented a variant of Myo$_{bLT}$ to investigate the effectiveness of the proposed fuse schema, i.e., MSF, on myocardium extraction.

- Myo$_{bLT}^{w/o\ MSF}$: Myo$_{bLT}$ which extracted myocardium of CRIs without fusing multi-sequence information via MSF.

TABLE IV: Performance of the different myocardium extraction methods. Subscript "$_{bL}$": bSSFP and LGE images; Subscript "$_{LT}$": LGE and T2 images; Subscript "$_{bLT}$": bSSFP, LGE and T2 images. NoS: Number of sequences. The best results are labeled in **bold**.

Method	Sequences				Myocardium	
	bSSFP	LGE	T2	NoS	Dice (%) ↑	HD (mm) ↓
Myo$_{bL}$	✓	✓	✗	2	83.39 (4.829)	18.23 (21.18)
Myo$_{LT}$	✗	✓	✓	2	83.72 (3.334)	16.15 (18.35)
Myo$_{bLT}$	✓	✓	✓	3	**85.87 (2.786)**	**9.238 (7.872)**
Myo$_{bLT}^{w/o\ MSF}$	✓	✓	✓	3	84.13 (4.544)	12.88 (16.86)

Table IV lists the results of different myocardium extraction methods. Overall, the method using three sequences (i.e., Myo$_{bLT}$) outperformed the methods using two sequences (i.e., Myo$_{bL}$ and Myo$_{LT}$). For example, Myo$_{bLT}$ improved the Dice and HD by almost 2% ($p < 0.01$) and 7 mm ($p = 0.07$) against Myo$_{LT}$, respectively. This demonstrated the advantage of aligning more sequences of images for myocardium extraction. Meanwhile, Fig. 12 visualizes different myocardium extraction results. One can observe the myocardial pathology regions easily degraded the myocardium extraction performance (see red Arrows). Whereas, Myo$_{bLT}$ obtained more plausible details than other methods by using three CMR sequences.

Furthermore, we investigated the effectiveness of MSF for myocardium extraction. Even Myo$_{bLT}^{w/o\ MSF}$ consumed three sequence images, it did not explicitly fuse multi-sequence feature maps for myocardium extraction. Based on MSF, Myo$_{bLT}$ could increased Dice by almost 2% ($p < 0.01$) against Myo$_{bLT}^{w/o\ MSF}$. In Fig. 12, one can also observe that Myo$_{bLT}$ achieved robust results than Myo$_{bLT}^{w/o\ MSF}$ (see orange Arrows).

Additionally, we visualized the procedure of fusing misaligned feature maps of MSF in Fig. 11. We first showed the corresponding feature maps (F_{bSSFP}, F_{T2} and F_{LGE}) of unaligned MS-CMR images (I_{bSSFP}, I_{T2} and I_{LGE}). For better demonstration, we placed a fixed spatial point q on each feature map. Initially, the semantic information of F_{bSSFP}, F_{T2} and F_{LGE} in q could be incorrectly integrated via existing fusion operations, such as channel-wise concatenation [40] and max-fusion [41]. Whereas MSF could fuse F_{bSSFP} (or F_{T2}) with F_{LGE} by transforming F_{bSSFP} (or F_{T2}) into $\tilde{F}_{bSSFP}$

(or $\tilde{F}_{T2}$). Therefore, MSF provided a more appropriate and reliable way to fuse multi-sequence information.
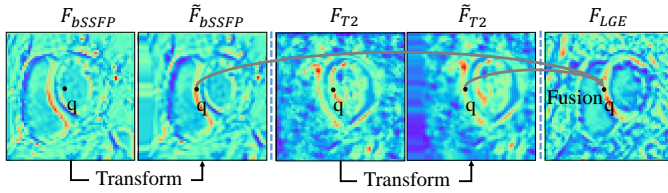
Fig. 11: Illustration of fusing the feature maps of multi-sequence cardiac magnetic resonance images via MSF. F_{bSSFP}, F_{T2} and F_{LGE} are the feature maps from 3-rd level of E_{bSSFP}, E_{T2} and E_{LGE}, respectively. $\tilde{F}_{bSSFP}$ and $\tilde{F}_{T2}$ are the spatially transformed of F_{bSSFP} and F_{T2}, respectively. Each q represents a point with a fixed spatial coordinate in feature maps. The semantic information of feature maps (i.e., $\tilde{F}_{bSSFP}$, $\tilde{F}_{T2}$ and F_{LGE}) in q could become consistent after transformation.
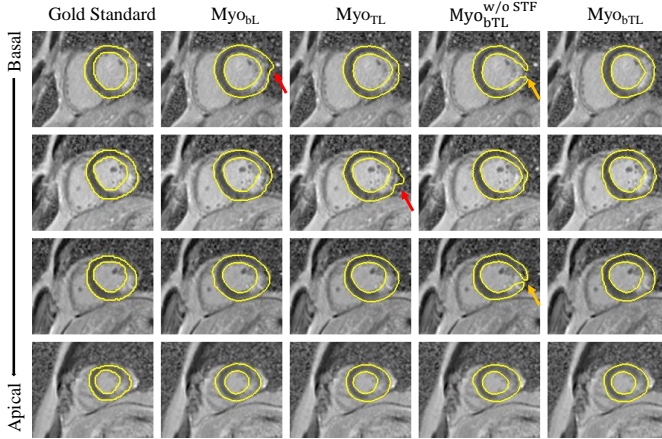
Fig. 12: Visualization of myocardium extraction results from basal to apical slices. The results are overlaid on common reference images (CRIs). Yellow curves indicate the predicted myocardium and gold standard myocardium contours of CRIs. Arrows point to myocardial pathology regions which could easily degrade myocardium extraction methods.

G. Results of Multi-Sequence Registration on pMM-CMR Dataset

We investigated the registration performance of U-MyoPS by comparing it with three state-of-the-art registration methods[7].

- ANTs [42]: One of the state-of-the-art conventional affine + deformable registration tools. We invoked *"SyN"* registration function based on their Python implementation.
- VoxelMorph [43]: One of the state-of-the art networks which could perform pair-wise registration. The network was mainly trained by Dice loss.

---

[7] ANTs: https://github.com/ANTsX/ANTsPy;
VoxelMorph: https://github.com/voxelmorph/voxelmorph;
RegNet_{mvmm}: https://github.com/xzluo97/MvMM-RegNet

- RegNet_{mvmm} [29]: The multi-sequence registration network which could jointly register MS-CMR images. The network was mainly trained based on MvMM loss function.
- U-MyoPS_{Reg}: The multi-sequence registration module of U-MyoPS.

Moreover, we implemented a variants of U-MyoPS_{Reg} to investigated the effectiveness of constraint loss [see (6)].

- U-MyoPS_{Reg}^{w/o Cons}: U-MyoPS_{Reg} without utilizing constraint loss during network training.

Table V summaries the registration results of different methods. One can observe that all registration methods could mitigate the misalignment among bSSFP, T2 and LGE images. Effectively, U-MyoPS_{Reg} obtained the best Dice and HD results among all the registration methods. Particularly, U-MyoPS_{Reg} obtained better Dice (6.2%, $p < 0.05$) and HD (9.4 mm, $p < 0.01$) performances than ANTs for T2 to LGE registration. Meanwhile, compared to RegNet_{mvmm}, U-MyoPS_{Reg} improved the Dice of bSSFP to LGE and T2 to LGE registration by 7.8% ($p < 0.01$) and 5.2% ($p < 0.01$), respectively. Furthermore, compared to the state-of-the-art registration network Voxelmorph, U-MyoPS_{Reg} obtained 2.4% ($p < 0.05$) and 2.7% ($p < 0.05$) Dice improvements for bSSFP to LGE and T2 to LGE registration, respectively. This indicated that U-MyoPS obtained promising performance for registration.

Moreover, the lower part of Table V presents the result of U-MyoPS_{Reg}^{w/o Cons}. Without constraint loss [see (6)], U-MyoPS_{Reg}^{w/o Cons} suffered performance degradation for registration. For instance, U-MyoPS_{Reg}^{w/o Cons} decreased Dice (2.5%, $p < 0.01$) and HD (0.65 mm, $p = 0.12$) for bSSFP to LGE registration. This implied the benefit of constraint loss.

TABLE V: The registration accuracy of different methods on myocardium. bSSFP→LGE: bSSFP to LGE registration; T2→LGE: T2 to LGE registration.

Method	bSSFP→LGE		T2→LGE	
	Dice (%) ↑	HD (mm) ↓	Dice (%) ↑	HD (mm) ↓
Initial	51.53 (18.01)	35.34 (40.34)	39.98 (18.04)	71.10 (98.52)
ANTs	78.44 (6.060)	10.80 (4.045)	73.11 (13.46)	18.85 (9.534)
RegNet_{mvmm}	71.21 (11.80)	12.41 (4.542)	74.05 (10.36)	11.79 (4.930)
Voxelmorph	76.63 (9.756)	12.89 (7.332)	76.55 (7.470)	14.45 (7.975)
U-MyoPS_{Reg}	**79.07 (5.060)**	**8.548 (2.001)**	**79.26 (4.824)**	**9.427 (3.398)**
U-MyoPS_{Reg}^{w/o Cons}	76.57 (5.893)	9.200 (2.354)	77.95 (6.663)	9.816 (3.974)

H. Correlation Study

U-MyoPS performed multi-sequence registration, myocardium extraction and MyoPS tasks. The multi-sequence registration and myocardium extraction could promote MyoPS task (see Section III-D.1). We further investigated the correlations among these tasks for U-MyoPS_{bLT}, and measured the correlations by calculating coefficient of determination (R^2).

1) Correlation between Multi-sequence Registration and MyoPS : R_{bSSFP} (or R_{T2}) predicted TPS transformation parameters to align bSSFP (or T2) to LGE images, and we measured the registration accuracy via the Dice between the myocardium label of the warped bSSFP (or T2) and LGE
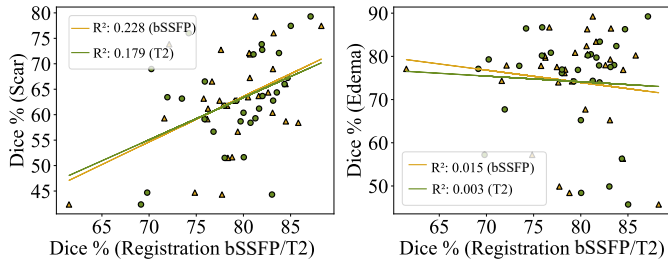
Fig. 13: Correlation between the accuracy of multi-sequence registration and MyOPS.

images. The left of Fig. 13 shows that the registration accuracy of bSSFP and T2 had a correlation to the scar segmentation. This is because that both the boundary and edema information in the warped bSSFP and T2 images would complement the scar segmentation. Fusing more accurate information could further improve the corresponding scar segmentation. Note that there was an insignificant relationship between the registration accuracy and edema segmentation as shown in the right of Fig. 13. This is probably because the multi-sequence registration of U-MyoPS has already achieved sufficient accuracy to fuse complementary and relevant information for edema segmentation.
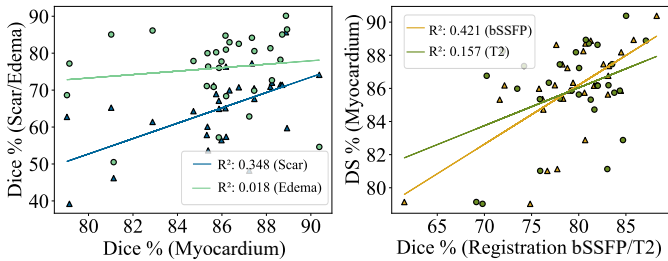

Fig. 14: Correlation between the accuracy of myocardium extraction and MyOPS .

Fig. 15: Correlation between the accuracy of multi-sequence registration and myocardium extraction.

2) Correlation between Myocardium Extraction and MyOPS:
Fig. 14 shows the scar segmentation had a correlation with the accuracy of myocardium extraction. This is reasonable as scars (in LGE images) can appear identical to surroundings (such as LV and RV blood pool) [13]. Thus myocardium contours were critical to distinguish scars from surroundings. Besides, the correlation between edema segmentation and myocardium extraction was insignificant. The potential reason is that U-MyoPS achieved sufficient myocardium extraction accuracy to promote edema segmentation. Meanwhile, the edema (in T2 images) were more easily distinguishable from the surroundings (such as LV and RV blood pool). Thus, the accuracy of edema segmentation would be less sensitive to the accuracy of myocardium extraction.

3) Correlation Between Multi-sequence Registration and Myocardium Extraction: Fig. 15 shows that both the registration accuracy of bSSFP and T2 images were correlated to myocardium extraction, while the registration accuracy of bSSFP
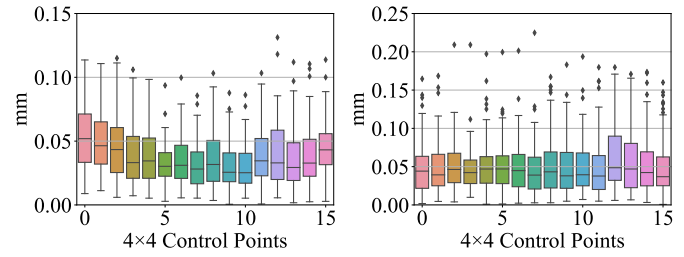
(a) Predicted displacement of R_{bSSFP} (b) Predicted displacement of R_{T2}

Fig. 16: Box plots of predicted TPS displacements on MYOPS2020 challenge dataset. For better demonstration, we normalized the displacements by dividing them by H and W, and obtained the L2 norm of normalized displacements. (a) and (b) visualize the predicted displacements of R_{bSSFP} and R_{T2}, respectively.

had more impact on myocardium extraction than the one of T2. This was reasonable as bSSFP images could provide clear boundary information, which was more important than T2 for myocardium extraction.

I. Results on Public MYOPS2020 Challenge Dataset

We performed MyOPS for MYOPS2020 challenge dataset via U-MyoPS$_{bLT}$. The gold standard pathology labels in the common space for evaluation were provided by MYOPS2020 challenge. Table VI summarizes segmentation results of U-MyoPS$_{bLT}$ as well as other state-of-the-art methods[8]. In this dataset, U-MyoPS$_{bLT}$ achieved third and second places for scar and edema segmentation, respectively. It is worth noting that U-MyoPS$_{bLT}$ obtained segmentation results without using model ensemble strategies, whereas top performance methods (i.e., UESTC*, UBA* and NPU*) achieved their results by using different model ensemble strategies [44]–[46]. The lower part (under the dashed line) of Table VI presents that U-MyoPS$_{bLT}$ obtained the best average results among all the comparison methods when discarding model ensemble strategies.

Additionally, Fig. 16 displays the statistic of predicted TPS displacements (see Eq. 1). One can see most of the displacements were less than 0.05 mm. Such a phenomenon is reasonable since MYOPS2020 challenge dataset was officially pre-aligned. Nevertheless, a few displacements were larger than 0.2 mm. This is probably due to the fact that some cases were not well aligned in the official MYOPS2020 challenge dataset [20]. U-MyoPS$_{bLT}$ could further alleviate the misalignment, as shown in Fig. 17.

IV. DISCUSSION AND CONCLUSION

This work presents an automatic combined computing framework, i.e., U-MyoPS, which could segment scar, edema and healthy myocardium within one unified result using practical unaligned MS-CMR images. To our best knowledge, existing DL-based MyoPS methods focused on processing aligned

---

[8] http://www.sdspeople.fudan.edu.cn/zhuangxiahai/0/myops20/result.html

TABLE VI: The Dice results of different methods on the testing set of MYOPS2020 challenge dataset. Superscript "*" indicates that the method employed a model ensemble strategy. The best and second metrics are labeled in **bold** and underline. The results of comparison methods were gathered from their official papers.

Method	Scar (%) ↑	Edema (%) ↑	Average (%) ↑
UESTC* [45]	**67.2**	**73.1**	**70.2**
UBA* [44]	<u>66.6</u>	69.8	68.2
NPU* [46]	64.7	70.9	67.8
UESTC [45]	64.1	69.5	66.8
NPU [46]	62.6	69.5	66.1
CQUPT II [47]	58.1	72.5	65.3
U-MyoPS$_{bLT}$	64.7	<u>72.6</u>	<u>68.6</u>
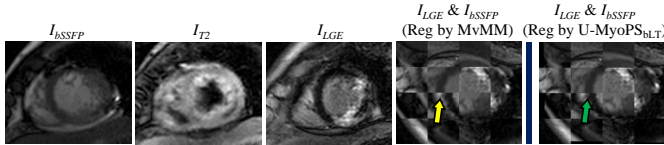
Fig. 17: A checkerboard visualization of multi-sequence cardiac magnetic resonance image registration result. The images are from #19 case of test dataset of MYOPS2020 challenge. After registering by MvMM, there may remain misalignment between I_{bSSFP} and I_{LGE} (see yellow Arrow). While, U-MyoPS$_{bLT}$ could further improve the official registration results (see green Arrow). Reg: Registered.

MS-CMR images [17], [20], [23]. U-MyoPS could segment myocardial pathologies from unaligned MS-CMR images in a fully automatic way, which could bring convenience to clinical practices. In U-MyoPS, we proposed a novel MSF for spatially unaligned feature map fusion. MSF could be considered as one of layer-level fusion schemes [48], [49]. In contrast to previous fusion strategies [41], [50]–[52], MSF provided a more appropriate way to aggregate spatially unaligned multi-sequence feature maps (see Fig. 11). Meanwhile, we introduced an SPG to propagate extracted myocardium to promote MyoPS (see Section III-D.2]). In experiments, we evaluated U-MyoPS on an unaligned MS-CMR dataset (see Table II) and a public pre-aligned MS-CMR dataset (see Table VI). The results demonstrated that U-MyoPS achieved comparable performance to existing MyoPS methods.

The main limitation of U-MyoPS is the lack of joint optimization of multi-tasks. During our training period, we simultaneously optimized the multi-sequence registration and myocardium extraction tasks, but independently optimized the pathology segmentation task. Actually, we had performed joint optimization of these three tasks but observed a performance decrease of the pathology segmentation task. This is because both multi-sequence registration and myocardium extraction tasks focused on structure information, so they collaborated with each other based on joint optimizations. Whereas the pathology segmentation task focused on the high-lighted abnormal intensity information, and thus it is still challenging to combine it with multi-sequence registration and myocardium

extraction tasks at present. Future work could pursue an end-to-end trainable framework.

Further improvements in U-MyoPS could be achieved by exploring the importance of each sequence. Note the effects of different sequences are varied. For example, aligning bSSFP and T2 images promoted scar segmentation (see Fig. 13). While the registration accuracy of bSSFP brought more benefit to scar segmentation than the one of T2. Thus, it is critical to estimate the reliability of each sequence for specific tasks. We can study dynamic methods for the weighted fusion of different images for a specific task in the future. Besides, there exist slice shifts due to breath-hold mis-registration in multi-slice CMR images, which could hinder myocardial pathology monitoring [53]. In future work, it is valuable to correct these shifts to promote U-MyoPS for clinical applications.

U-MyoPS is a new technique to perform myocardial pathology segmentation from unaligned MS-CMR images. Aligning MS-CMR images could promote MyoPS performance. There exist three key points, i.e., accuracy, time efficiency and generalizability, to consider in determining whether MyoPS algorithms fit for the clinical workflow [20]. For accuracy, U-MyoPS could achieve agreements with manual delineation for scar size, scar transmurality and edema size quantification. For time efficiency, U-MyoPS consumed 10 seconds to segment pathologies from unaligned MS-CMR images, which was efficient for clinical applications. Nevertheless, for generalizability, U-MyoPS would suffer performance degradation when the test data acquisition protocol differs significantly from the training data acquisition protocol [54], [55]. Therefore, we need to further improve the generalization ability of U-MyoPS before it could be applied for routine clinical assessment.

REFERENCES

[1] G. W. Reed, J. E. Rossi, and C. P. Cannon, "Acute myocardial infarction," *The Lancet*, vol. 389, no. 10065, pp. 197–210, 2017.

[2] K. Thygesen, J. S. Alpert, A. S. Jaffe, B. R. Chaitman, J. J. Bax, D. A. Morrow, H. D. White, and E. G. on behalf of the Joint European Society of Cardiology (ESC)/American College of Cardiology (ACC)/American Heart Association (AHA)/World Heart Federation (WHF) Task Force for the Universal Definition of Myocardial Infarction, "Fourth universal definition of myocardial infarction (2018)," *Journal of the American College of Cardiology*, vol. 72, no. 18, pp. 2231–2264, 2018.

[3] F. Guo, P. R. Krahn, T. Escartin, I. Roifman, and G. Wright, "Cine and late gadolinium enhancement MRI registration and automated myocardial infarct heterogeneity quantification," *Magnetic Resonance in Medicine*, vol. 85, no. 5, pp. 2842–2855, 2021.

[4] A. Kolipaka, G. P. Chatzimavroudis, R. D. White, T. P. O'Donnell, and R. M. Setser, "Segmentation of non-viable myocardium in delayed enhancement magnetic resonance images," *The international journal of cardiovascular imaging*, vol. 21, no. 2-3, pp. 303–311, 2005.

[5] L. C. Amado, B. L. Gerber, S. N. Gupta, D. W. Rettmann, G. Szarf, R. Schock, K. Nasir, D. L. Kraitchman, and J. A. Lima, "Accurate and objective infarct sizing by contrast-enhanced magnetic resonance imaging in a canine myocardial infarction model," *Journal of the American College of Cardiology*, vol. 44, no. 12, pp. 2383–2389, 2004.

[6] X. Albà, R. M. F. i Ventura, K. Lekadir, and A. F. Frangi, "Healthy and scar myocardial tissue classification in DE-MRI," in *International Workshop on Statistical Atlases and Computational Models of the Heart*, pp. 62–70, Springer, 2012.

[7] Y. Lu, Y. Yang, K. A. Connelly, G. A. Wright, and P. E. Radau, "Automated quantification of myocardial infarction using graph cuts on contrast delayed enhanced magnetic resonance images," *Quantitative imaging in medicine and surgery*, vol. 2, no. 2, p. 81, 2012.

[8] G. Litjens, T. Kooi, B. E. Bejnordi, A. A. A. Setio, F. Ciompi, M. Ghafoorian, J. A. Van Der Laak, B. Van Ginneken, and C. I. Sánchez, "A survey on deep learning in medical image analysis," *Medical image analysis*, vol. 42, pp. 60–88, 2017.

[9] L. Li, V. A. Zimmer, J. A. Schnabel, and X. Zhuang, "Medical image analysis on left atrial LGE MRI for atrial fibrillation studies: A review," *Medical Image Analysis*, p. 102360, 2022.

[10] A. S. Fahmy, U. Neisius, R. H. Chan, E. J. Rowin, W. J. Manning, M. S. Maron, and R. Nezafat, "Three-dimensional deep convolutional neural networks for automated myocardial scar quantification in hypertrophic cardiomyopathy: a multicenter multivendor study," *Radiology*, vol. 294, no. 1, pp. 52–60, 2020.

[11] H. O'Brien, J. Whitaker, B. S. Sidhu, J. Gould, T. Kurzendorfer, M. D. O'Neill, R. Rajani, K. Grigoryan, C. A. Rinaldi, J. Taylor, *et al.*, "Automated left ventricle ischemic scar detection in ct using deep neural networks," *Frontiers in cardiovascular medicine*, vol. 8, 2021.

[12] F. Zabihollahy, J. A. White, and E. Ukwatta, "Convolutional neural network-based approach for segmentation of left ventricle myocardial scar from 3d late gadolinium enhancement mr images," *Medical physics*, vol. 46, no. 4, pp. 1740–1751, 2019.

[13] X. Zhuang, "Multivariate mixture model for myocardial segmentation combining multi-source images," *IEEE transactions on pattern analysis and machine intelligence*, vol. 41, no. 12, pp. 2933–2946, 2019.

[14] Q. Yue, X. Luo, Q. Ye, L. Xu, and X. Zhuang, "Cardiac segmentation from LGE MRI using deep neural network incorporating shape and spatial priors," in *International Conference on Medical Image Computing and Computer-Assisted Intervention*, pp. 559–567, Springer, 2019.

[15] F. Zabihollahy, M. Rajchl, J. A. White, and E. Ukwatta, "Fully automated segmentation of left ventricular scar from 3d late gadolinium enhancement magnetic resonance imaging using a cascaded multi-planar U-Net (CMPU-Net)," *Medical Physics*, vol. 47, no. 4, pp. 1645–1655, 2020.

[16] M. Lin, M. Jiang, M. Zhao, E. Ukwatta, J. White, and B. Chiu, "Cascaded triplanar autoencoder m-net for fully automatic segmentation of left ventricle myocardial scar from three-dimensional late gadolinium-enhanced mr images," *IEEE Journal of Biomedical and Health Informatics*, 2022.

[17] L. Li, W. Ding, L. Huang, X. Zhuang, and V. Grau, "Multi-modality cardiac image computing: A survey," *arXiv preprint arXiv:2208.12881*, 2022.

[18] M. G. Friedrich, "Myocardial edema—a new clinical entity?," *Nature Reviews Cardiology*, vol. 7, no. 5, pp. 292–296, 2010.

[19] X. Zhuang, L. Li, F. Wu, X. Luo, Y. Zhou, and J. Xu, "Myops 2020: Myocardial pathology segmentation combining multi-sequence cmr." http://www.sdspeople.fudan.edu.cn/zhuangxiahai/0/myops20/people.html, 2023 (accessed January 30, 2023).

[20] L. Li, F. Wu, S. Wang, X. Luo, C. Martin-Isla, S. Zhai, J. Zhang, Y. Liu, Z. Zhang, M. J. Ankenbrand, *et al.*, "MyoPS: A benchmark of myocardial pathology segmentation combining three-sequence cardiac magnetic resonance images," *arXiv preprint arXiv:2201.03186*, 2022.

[21] A. S. Fahmy, E. J. Rowin, R. H. Chan, W. J. Manning, M. S. Maron, and R. Nezafat, "Improved quantification of myocardium scar in late gadolinium enhancement images: Deep learning based image fusion approach," *Journal of Magnetic Resonance Imaging*, 2021.

[22] X. Zhuang and L. Li, *Myocardial Pathology Segmentation Combining Multi-Sequence Cardiac Magnetic Resonance Images: First Challenge, MyoPS 2020, Held in Conjunction with MICCAI 2020, Lima, Peru, October 4, 2020, Proceedings*, vol. 12554. Springer Nature, 2020.

[23] K.-N. Wang, X. Yang, J. Miao, L. Li, J. Yao, P. Zhou, W. Xue, G.-Q. Zhou, X. Zhuang, and D. Ni, "Awsnet: An auto-weighted supervision attention network for myocardial scar and edema segmentation in multi-sequence cardiac magnetic resonance images," *Medical Image Analysis*, p. 102362, 2022.

[24] D. Li, Y. Peng, Y. Guo, and J. Sun, "TAUNet: a triple-attention-based multi-modality MRI fusion U-Net for cardiac pathology segmentation," *Complex & Intelligent Systems*, pp. 1–17, 2022.

[25] I. Rocco, R. Arandjelovic, and J. Sivic, "Convolutional neural network architecture for geometric matching," in *Proceedings of the IEEE conference on computer vision and pattern recognition*, pp. 6148–6157, 2017.

[26] M. Jaderberg, K. Simonyan, A. Zisserman, *et al.*, "Spatial transformer networks," *Advances in neural information processing systems*, vol. 28, pp. 2017–2025, 2015.

[27] F. L. Bookstein, "Principal warps: Thin-plate splines and the decomposition of deformations," *IEEE Transactions on pattern analysis and machine intelligence*, vol. 11, no. 6, pp. 567–585, 1989.

[28] Y. Hu, M. Modat, E. Gibson, W. Li, N. Ghavami, E. Bonmati, G. Wang, S. Bandula, C. M. Moore, M. Emberton, *et al.*, "Weakly-supervised convolutional neural networks for multimodal image registration," *Medical image analysis*, vol. 49, pp. 1–13, 2018.

[29] X. Luo and X. Zhuang, "Mvmm-regnet: A new image registration framework based on multivariate mixture model and neural network estimation," in *International Conference on Medical Image Computing and Computer-Assisted Intervention*, pp. 149–159, Springer, 2020.

[30] R. R. Upendra, R. Simon, and C. A. Linte, "Joint deep learning framework for image registration and segmentation of late gadolinium enhanced mri and cine cardiac mri," in *Medical Imaging 2021: Image-Guided Procedures, Robotic Interventions, and Modeling*, vol. 11598, pp. 96–103, SPIE, 2021.

[31] C. Qin, W. Bai, J. Schlemper, S. E. Petersen, S. K. Piechnik, S. Neubauer, and D. Rueckert, "Joint learning of motion estimation and segmentation for cardiac mr image sequences," in *International Conference on Medical Image Computing and Computer-Assisted Intervention*, pp. 472–480, Springer, 2018.

[32] O. Ronneberger, P. Fischer, and T. Brox, "U-net: Convolutional networks for biomedical image segmentation," in *International Conference on Medical image computing and computer-assisted intervention*, pp. 234–241, Springer, 2015.

[33] P. A. Yushkevich, J. Piven, H. C. Hazlett, R. G. Smith, S. Ho, J. C. Gee, and G. Gerig, "User-guided 3d active contour segmentation of anatomical structures: significantly improved efficiency and reliability," *Neuroimage*, vol. 31, no. 3, pp. 1116–1128, 2006.

[34] I. Eitel and M. G. Friedrich, "T2-weighted cardiovascular magnetic resonance in acute cardiac disease," *Journal of Cardiovascular Magnetic Resonance*, vol. 13, no. 1, pp. 1–11, 2011.

[35] L. Li, W. Ding, L. Huang, and X. Zhuang, "Right ventricular segmentation from short-and long-axis mris via information transition," in *International Workshop on Statistical Atlases and Computational Models of the Heart*, pp. 259–267, Springer, 2021.

[36] F. Isensee, P. F. Jaeger, S. A. Kohl, J. Petersen, and K. H. Maier-Hein, "nnU-Net: a self-configuring method for deep learning-based biomedical image segmentation," *Nature methods*, vol. 18, no. 2, pp. 203–211, 2021.

[37] O. Bondarenko, A. M. Beek, M. B. Hofman, H. P. Kühl, J. W. Twisk, W. G. Van Dockum, C. A. Visser, and A. C. Van Rossum, "Standardizing the definition of hyperenhancement in the quantitative assessment of infarct size and myocardial viability using delayed contrast-enhanced cmr," *Journal of Cardiovascular Magnetic Resonance*, vol. 7, no. 2, pp. 481–485, 2005.

[38] F. H. Sheehan, E. L. Bolson, H. T. Dodge, D. G. Mathey, J. Schofer, and H. Woo, "Advantages and applications of the centerline method for characterizing regional ventricular function.," *Circulation*, vol. 74, no. 2, pp. 293–305, 1986.

[39] Q. Zhang, M. K. Burrage, M. Shanmuganathan, R. A. Gonzales, E. Lukaschuk, K. E. Thomas, R. Mills, J. Leal Pelado, C. Nikolaidou, I. A. Popescu, *et al.*, "Artificial intelligence for contrast-free mri: Scar assessment in myocardial infarction using deep learning–based virtual native enhancement," *Circulation*, vol. 146, no. 20, pp. 1492–1503, 2022.

[40] F. Li and W. Li, "Dual-path feature aggregation network combined multi-layer fusion for myocardial pathology segmentation with multi-sequence cardiac mr," in *Myocardial pathology segmentation combining multi-sequence CMR challenge*, pp. 146–158, Springer, 2020.

[41] H. Jiang, C. Wang, A. Chartsias, and S. A. Tsaftaris, "Max-fusion u-net for multi-modal pathology segmentation with attention and dynamic resampling," in *Myocardial pathology segmentation combining multi-sequence CMR challenge*, pp. 68–81, Springer, 2020.

[42] B. B. Avants, N. Tustison, and G. Song, "Advanced normalization tools (ANTS)," *Insight j*, vol. 2, no. 365, pp. 1–35, 2009.

[43] G. Balakrishnan, A. Zhao, M. R. Sabuncu, J. Guttag, and A. V. Dalca, "Voxelmorph: a learning framework for deformable medical image registration," *IEEE transactions on medical imaging*, vol. 38, no. 8, pp. 1788–1800, 2019.

[44] C. Martín-Isla, M. Asadi-Aghbolaghi, P. Gkontra, V. M. Campello, S. Escalera, and K. Lekadir, "Stacked BCDU-net with semantic CMR synthesis: Application to myocardial pathology segmentation challenge," in *Myocardial Pathology Segmentation Combining Multi-Sequence CMR Challenge*, pp. 1–16, Springer, 2020.

[45] S. Zhai, R. Gu, W. Lei, and G. Wang, "Myocardial edema and scar segmentation using a coarse-to-fine framework with weighted ensemble," in *Myocardial pathology segmentation combining multi-sequence CMR challenge*, pp. 49–59, Springer, 2020.

[46] J. Zhang, Y. Xie, Z. Liao, J. Verjans, and Y. Xia, "Efficientseg: A simple but efficient solution to myocardial pathology segmentation challenge,"

in *Myocardial pathology segmentation combining multi-sequence CMR challenge*, pp. 17–25, Springer, 2020.

[47] W. Li, L. Wang, and S. Qin, "CMS-UNet: Cardiac multi-task segmentation in MRI with a u-shaped network," in *Myocardial Pathology Segmentation Combining Multi-Sequence CMR Challenge*, pp. 92–101, Springer, 2020.

[48] T. Zhou, S. Ruan, and S. Canu, "A review: Deep learning for medical image segmentation using multi-modality fusion," *Array*, vol. 3, p. 100004, 2019.

[49] D. Ramachandram and G. W. Taylor, "Deep multimodal learning: A survey on recent advances and trends," *IEEE signal processing magazine*, vol. 34, no. 6, pp. 96–108, 2017.

[50] J. Dolz, K. Gopinath, J. Yuan, H. Lombaert, C. Desrosiers, and I. B. Ayed, "HyperDense-Net: a hyper-densely connected CNN for multimodal image segmentation," *IEEE transactions on medical imaging*, vol. 38, no. 5, pp. 1116–1126, 2018.

[51] T. Zhou, S. Ruan, Y. Guo, and S. Canu, "A multi-modality fusion network based on attention mechanism for brain tumor segmentation," in *2020 IEEE 17th international symposium on biomedical imaging (ISBI)*, pp. 377–380, IEEE, 2020.

[52] W. Lv, S. Ashrafinia, J. Ma, L. Lu, and A. Rahmim, "Multi-level multi-modality fusion radiomics: application to pet and ct imaging for prognostication of head and neck cancer," *IEEE journal of biomedical and health informatics*, vol. 24, no. 8, pp. 2268–2277, 2019.

[53] K. Gilbert, W. Bai, C. Mauger, P. Medrano-Gracia, A. Suinesiaputra, A. M. Lee, M. M. Sanghvi, N. Aung, S. K. Piechnik, S. Neubauer, *et al.*, "Independent left ventricular morphometric atlases show consistent relationships with cardiovascular risk factors: a uk biobank study," *Scientific reports*, vol. 9, no. 1, pp. 1–9, 2019.

[54] K. Zhou, Z. Liu, Y. Qiao, T. Xiang, and C. C. Loy, "Domain generalization: A survey," *IEEE Transactions on Pattern Analysis and Machine Intelligence*, 2022.

[55] C. Pei, F. Wu, L. Huang, and X. Zhuang, "Disentangle domain features for cross-modality cardiac image segmentation," *Medical Image Analysis*, vol. 71, p. 102078, 2021.